

HI Imaging of a Blueberry Galaxy Suggests a Merger Origin

Saili Dutta¹, Apurba Bera^{2,3}, Omkar Bait⁴, Chaitra A. Narayan¹, Biny Sebastian⁵, Sravani Vaddi⁶

¹ National Centre for Radio Astrophysics, Tata Institute of Fundamental Research, Pune University Campus, Pune 411007, India

² International Centre for Radio Astronomy Research, Curtin University, Bentley, WA 6102, Australia

³ Inter-University Centre for Astronomy and Astrophysics, Pune University Campus, Pune 411007, India

⁴ Observatoire de Genève, Université de Genève, 51 Ch. des Maillettes, 1290 Versoix, Switzerland

⁵ Department of Physics and Astronomy, University of Manitoba, Winnipeg, MB R3T 2N2, Canada

⁶ Arecibo Observatory, NAIC, HC3 Box 53995, Arecibo, Puerto Rico, PR 00612, USA

13 June 2024

ABSTRACT

Blueberry galaxies (BBs) are fainter, less massive, and lower redshift counterparts of the Green pea galaxies. They are thought to be the nearest analogues of the high redshift Lyman Alpha ($\text{Ly}\alpha$) emitters. We report the interferometric imaging of HI 21 cm emission from a Blueberry galaxy, J1509+3731, at redshift, $z = 0.03259$, using the Giant Metrewave Radio Telescope (GMRT). We find that this Blueberry galaxy has an HI mass of $M_{\text{HI}} \approx 3 \times 10^8 M_{\odot}$ and an HI-to-stellar mass ratio $M_{\text{HI}}/M_* \approx 2.4$. Using SFR estimates from the $\text{H}\beta$ emission line, we find that it has a short HI depletion time scale of ≈ 0.2 Gyr, which indicates a significantly higher star-formation efficiency compared to typical star-forming galaxies at the present epoch. Interestingly, we find an offset of ≈ 2 kpc between the peak of the HI 21 cm emission and the optical centre which suggests a merger event in the past. Our study highlights the important role of mergers in triggering the starburst in BBs and their role in the possible leakage of Lyman- α and Lyman-continuum photons which is consistent with the previous studies on BB galaxies.

Key words: galaxies: dwarf — galaxies: high-redshift — galaxies: ISM — galaxies: starburst — galaxies: star formation

1 INTRODUCTION

In the current understanding of the Λ -Cold Dark Matter (Λ CDM) cosmology, the structure formation in the Universe follows a hierarchical process. This bottom-up structure formation starts with small over-densities, the dwarf galaxies. Later massive galaxies grow from assembling these smaller galaxies through mergers and other accretion activities. A fraction of these low-mass young star-forming galaxies are the Lyman Alpha ($\text{Ly}\alpha$) emitters (LAEs); Lyman continuum (LyC) photons leaked by these LAEs are thought to be the main contributors in reionizing the Universe (Bouwens et al. 2015; Dressler et al. 2015; Drake et al. 2017; Dayal et al. 2020). Most known LAEs are high redshift, chemically less evolved, compact galaxies with low stellar mass, less dust, and a high ionization ratio. They are thought to be the progenitors of present-day Milky Way like galaxies, and provide an important probe to the earliest era of galaxy formation and the epoch of reionization (Finkelstein et al. 2007; Gawiser et al. 2007; Nakajima et al. 2012; Malhotra et al. 2012; Nakajima & Ouchi 2014; Yang et al. 2017a; Naka-

jima et al. 2020). Detailed study of the inter-stellar medium (ISM) of LAEs is difficult because most LAEs are distant high redshift galaxies. However, identification of low redshift LAE-analogues allows us to indirectly probe the ISM properties of distant LAEs.

The Galaxy Zoo project (Lintott et al. 2008) identifies a class of green-colored, small-sized objects from the Sloan Digital Sky Survey Data Release 7 (SDSS DR7; Abazajian, et al. 2009), known as the "Green Pea" galaxies (GPs). These highly star-forming ($\text{SFR} \sim 10 M_{\odot} \text{yr}^{-1}$) galaxies have high specific star formation rates ($\text{sSFR} \sim 10 \text{Gyr}^{-1}$) for their stellar masses ($\log[M_*/M_{\odot}] \sim 8 - 10$), low metallicities ($12 + \log[\text{O}/\text{H}] \sim 8.05$) and high $[\text{O III}]\lambda 5007/[\text{O II}]\lambda 3727$ (O32) ratios (Cardamone et al. 2009; Amorín, Pérez-Montero, & Vílchez 2010; Amorín et al. 2012; Jaskot & Oey 2014; Izotov, Guseva, & Thuan 2011). The bright green color of these compact galaxies arises from very strong $[\text{O III}]\lambda 5007$ emission line with large equivalent widths ($\sim 1000 \text{\AA}$) which falls into the SDSS 'r' band. After the discovery of these GPs, several studies have brought forward interesting similarities between these GPs and the

high redshift LAEs (Henry et al. 2015; Yang et al. 2016, 2017a; Izotov et al. 2020). Jaskot & Oey (2014) suggest that GPs are optically thin systems, which makes it possible for the LyC photons to escape. The results from Henry et al. (2015) support this scenario indicating to low atomic hydrogen (HI) column densities in GPs. Outcomes of several studies on Ly α profiles, Ly α and LyC escape fractions of GPs (Yang et al. 2016, 2017a; Izotov et al. 2016a,b, 2018; Loft-house, Houghton, & Kaviraj 2017; McKinney et al. 2019) strengthened the hypothesis that GPs are local analogues of high redshift LAEs. Importantly, it has been found that GPs can leak a significant fraction of LyC photons, making them similar to early star-forming galaxies believed to be responsible for reionization of the Universe (e.g., Izotov et al. 2016a,b). Several high-redshift ($z > 6$) galaxies, recently detected by James Webb Space Telescope (JWST), show properties very similar to GPs, thus increasing our confidence of them being good local analogues to early star-forming galaxies (Schaerer et al. 2022; Rhoads et al. 2023; Cameron et al. 2023; Matthee et al. 2022).

Yang et al. (2017b) (hereafter, Y17) present 40 starburst dwarf galaxies from SDSS Data Release 12 (SDSS DR12; Alam et al. 2015) catalogue¹ with redshifts $z \leq 0.05$ and similar properties as GPs. The [O III] $\lambda 5007$ emission lines from these galaxies fall into the SDSS ‘g’ band (because of their lower redshifts), giving blue colours to the composite images, and leading to the name “Blueberry” Galaxies (BBs). Later it has become a convention to refer all these low redshift analogues of LAEs as “Green Pea” galaxies. However, we follow the traditional nomenclature and refer the lower redshift ($z < 0.1$) galaxies with blue-coloured composite images as “Blueberry” galaxies. These BBs represent fainter, less massive, and lower redshift counterparts of the GPs, and are thought to be the nearest analogues of the high redshift LAEs. A radio continuum study of some of these BBs shows suppression in the radio-based SFR compared to the optical SFR estimates (Sebastian & Bait 2019).

Jiang et al. (2019) present a collection of 835 GPs from SDSS DR13 (Albareti et al. 2017) within the redshift range $0.011 < z < 0.411$. Kanekar et al. (2021) (hereafter, K21) select 40 galaxies from the sample of Jiang et al. (2019) at $z < 0.1$ and report the first detection of HI 21 cm line emission in 19 GPs (we refer to these as BBs in this article as per the traditional nomenclature) along with estimates of their HI masses using the Arecibo Telescope or the Green Bank Telescope (GBT). They also find a lower HI detection rate for galaxies with higher O32 ratios. Purkayastha et al. (2022) present the first interferometric HI 21 cm imaging of a BB galaxy using the Giant Metrewave Radio Telescope (GMRT), which suggests a galaxy-galaxy merger event to be the reason for the starburst activity.

Here we present, HI 21 cm imaging of a Blueberry galaxy, J1509+3731, at redshift² $z = 0.03259$. We describe the observations and data reduction process in Section 2. The observed HI properties of the Blueberry galaxy are described in Section 3. The implications of the observed HI

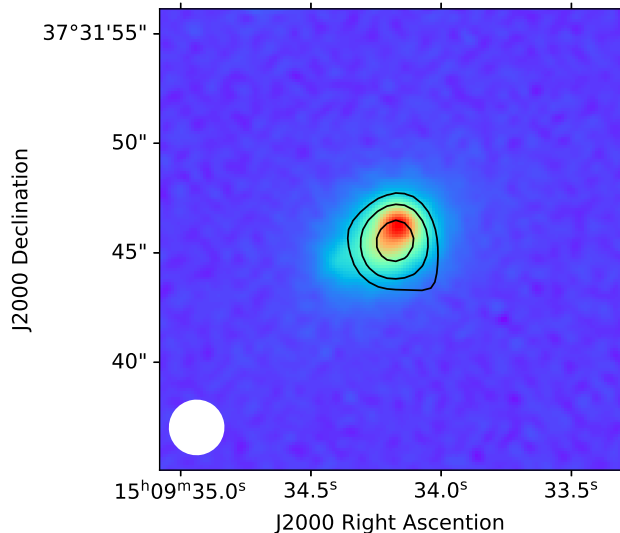


Figure 1. Radio continuum emission from BB10: The 1.4 GHz radio continuum contours are overlaid on the DESI Legacy Survey g-band image. The contour levels are at 4, 8, and 16 times the RMS noise of the radio image. The synthesized beam of the radio image ($2.5'' \times 2.5''$) is shown at the bottom left corner. The radio emission is resolved with a source size of $\approx 5''$, about the same as the optical diameter of the galaxy.

properties, in the context of high redshift LAEs, are discussed in Section 4. Finally, we summarize our results and conclusions in Section 5.

2 OBSERVATIONS AND DATA ANALYSIS

2.1 The target galaxy

We select J1509+3731 (hereafter BB10) with J2000 coordinates $RA = 15^h 09^m 34.17^s$, $DEC = +37^d 31' 46.1''$ from Y17 as the target galaxy for HI 21 cm observation with the GMRT. The redshift of BB10 is $z = 0.03259 (\pm 0.00001)$, which corresponds to a distance of 144 Mpc. The optical properties of BB10 are compiled in Table 1. It has a high specific star formation rate ($\approx 13 \text{ Gyr}^{-1}$) and a very high O32 ratio (≈ 15.7). In addition to these, its low metallicity and small optical size make it an ideal candidate to study as a local analogue of high redshift LAEs. Importantly, this galaxy shows strong Ly α emission and also evidence of Ly α absorption in the Hubble Space Telescope (HST) Cosmic Origins Spectrograph (COS) spectrum presented by Jaskot et al. (2019). The Ly α emission features show two peaks with a large Ly α peak velocity separation of $\Delta v_{\text{Ly}\alpha} = 400 \pm 27 \text{ km s}^{-1}$ and a weak Ly α escape fraction of $f_{\text{esc}}^{\text{Ly}\alpha} = 0.05 \pm 0.03$ (Jaskot et al. 2019). Previously, K21 targeted this galaxy using GBT and provided an upper limit (3σ) on the HI mass, $M_{\text{HI}} < 4.4 \times 10^8 M_{\odot}$.

2.2 Observations and Data Analysis

The target galaxy, BB10, was observed with the band-5 (1000-1450 MHz) system of the upgraded GMRT (uGMRT), under the observing proposal DDTC095 (PI: Chaitra A.

¹ <https://www.sdss4.org/dr12/>

² We assume a flat Λ CDM cosmology with $(\Omega_m, \Omega_{\Lambda}, h) = (0.315, 0.685, 0.674)$ (Planck Collaboration et al. 2020), where h is the dimensionless Hubble parameter related to the Hubble Constant $H_0 = 100 h \text{ km s}^{-1} \text{ Mpc}^{-1}$.

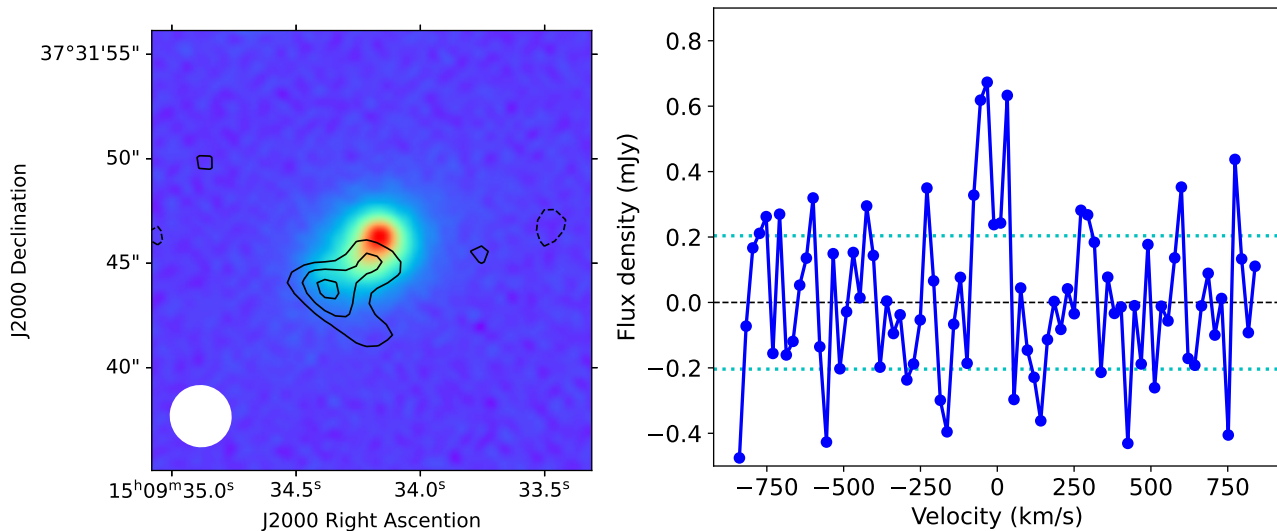


Figure 2. [A, left] HI 21 cm emission map of BB10 at a resolution of $2.9''$: The HI contours, corresponding to the emission map obtained by averaging six central velocity channels within the FWHM of the HI 21 cm signal, are overlaid on the DESI Legacy Survey g-band image. The contour levels are at 2, 3, and 4 times the RMS noise in the HI 21 cm emission map. The negative contours are shown in dashed lines. The synthesized beam is shown at the bottom left corner. [B, right] Spatially integrated HI 21 cm emission spectrum of BB10 at a velocity resolution of 21.8 km s^{-1} : The HI 21 cm spectrum has been integrated over the region within the outermost contour on the left plot. The dotted line shows the spectral RMS noise.

M_* $\times 10^8 M_\odot$	SFR $M_\odot \text{ yr}^{-1}$	O32	$12 + \log[O/H]$
1.26	1.61	15.67	7.87

Table 1. The properties of J1509+3731 (BB10) from Yang et al. (2017b). The columns are i) stellar mass, ii) star formation rate, iii) O32 ratio, and iv) metallicity.

Narayan), for a total on-source time of ~ 9 hrs. The observations were carried out with a bandwidth of 100 MHz (divided into 8192 channels) centered at 1380.00 MHz, using the GMRT Wideband Backend (GWB). Radio sources 3C286 and 1602+334 were used as the flux and the phase calibrator, respectively. The central square baselines, for the GWB system, were affected by a power-offset³. Hence the central square baselines were excluded from our analysis.

2.3 Radio continuum imaging

Radio interferometric imaging was carried out using the CASA (Common Astronomy Software Applications) software package (McMullin et al. 2007). After gain calibration and bandpass calibration using the flux calibrator, visibility data were inspected for the presence of radio frequency interference (RFI). Following the excision of RFI-affected data, visibilities were averaged to 781 kHz frequency channels for continuum imaging. Channels within $\pm 200 \text{ km s}^{-1}$ of the expected location of the HI 21 cm line were not used for continuum imaging. The continuum image was made using the task TCLEAN, and was used to self-calibrate the visibility

data. The final continuum image has an RMS noise of $12.4 \mu\text{Jy beam}^{-1}$ and an angular resolution of $2.5'' \times 2.5''$.

Radio continuum emission from BB10 was detected in our continuum image, as shown in Figure 1 where we plot the 1.4 GHz radio continuum contours on the optical g-band image⁴ from Dark Energy Spectroscopic Instrument (DESI) Legacy imaging survey (Dey et al. 2019). We used the CASA task IMFIT to estimate the properties of the emission source by fitting a 2-dimensional elliptical Gaussian to the spatial brightness distribution. A detailed description of the task, and the algorithms used, can be found in the CASA documentation⁵. The uncertainties on the flux density and the sky position of the peak are estimated using the prescription of Condon et al. (1997).

The radio continuum emission is marginally resolved⁶ with an integrated 1.4 GHz flux density of $340 \pm 29 \mu\text{Jy}$. Our estimate of the (integrated) flux density is consistent with its previously published measurement ($345 \pm 16 \mu\text{Jy}$; Sebastian & Bait 2019). The peak flux density of the radio continuum emission (at an angular resolution of $2.5''$) is $261 \mu\text{Jy beam}^{-1}$, detected at a statistical significance of $(S/N)_{\text{peak}} = 21$ (i.e. peak / RMS noise).

The uncertainties on the sky position of the peak of the emission source is given by (Condon et al. 1997, 1998)

⁴ <https://www.legacysurvey.org/>

⁵ <https://casadocs.readthedocs.io/en/latest/api/tt/casatasks.analysis.imfit.html>

⁶ The peak flux density and the integrated flux density of the source differ by $\approx 2.5\sigma$. It has a deconvolved size of $1.6'' \times 1.0''$, which is smaller than the synthesized beam. We verified these estimates by performing source extraction using a different software package (PyBDSF; Mohan & Rafferty 2015), which yielded consistent results.

³ A detailed description of the issue can be found at http://gmrt.ncra.tifr.res.in/gmrt_users/help/csq_baselines.html.

$$\Delta\text{RA} \approx \Delta\text{DEC} \approx \frac{\Theta_{\text{FWHM}}}{2(\text{S/N})_{\text{peak}}} \quad (1)$$

where Θ_{FWHM} is the FWHM of the synthesized beam and $(\text{S/N})_{\text{peak}}$ is the ratio of the peak flux density (not the spatially integrated flux density) to RMS noise. For example, the sky position of a source with a peak $\text{S/N} = 5$ can be measured with an accuracy of approximately a tenth of the FWHM of the synthesized beam in each of RA and DEC (Condon et al. 1998).

The peak of the radio continuum emission associated with BB10 is offset by $0.7'' \pm 0.1''$ (0.49 ± 0.06 kpc) from the peak of optical emission (see Figure 1). The uncertainties on the position of the radio peak is consistent with the relation in Equation 1. To investigate any systematic spatial offset in our radio image, we compared the positions of bright compact sources in our continuum image (within the FWHM of the GMRT primary beam) with their reference positions in the NRAO VLA Sky Survey (NVSS⁷; Condon et al. 1998) catalogue. The individual offsets along RA and DEC, i.e. $\delta\text{RA} = \text{RA} - \text{RA}_{\text{NVSS}}$ and $\delta\text{DEC} = \text{DEC} - \text{DEC}_{\text{NVSS}}$, are randomly distributed with both positive and negative values, around their median values of $\delta\text{RA}_{\text{median}} = 0.1''$ and $\delta\text{DEC}_{\text{median}} = 0.04''$. Note that $\delta\text{RA}_{\text{median}}$ and $\delta\text{DEC}_{\text{median}}$, the median values of the offsets along RA and DEC, represent the systematic offset between our radio image and NVSS. This systematic offset is significantly smaller than the offset between the radio and the optical peaks, and hence we do not apply any correction for the systematic offset.

2.4 Spectroscopic imaging

The gain solutions from self-calibration were applied to visibilities at the native frequency resolution (before channel averaging). After another round of RFI excision, the calibrated visibilities were used to make HI 21 cm data cube with a velocity resolution of 21.8 km s^{-1} . The HI data cube was made using visibilities with a UV upper limit of $60 \text{ k}\lambda$ (and Briggs weighting scheme, with $\text{robust} = 1.0$), which yielded a spatial resolution of $2.9'' \times 2.9''$. The RMS noise at this angular resolution, per 21.8 km s^{-1} velocity channel, is $\approx 170 \mu\text{Jy beam}^{-1}$. A spectral baseline was subtracted from each spatial pixel in the cube, where the spectral baseline was obtained by fitting a second-order polynomial to the spectra excluding channels within $\pm 200 \text{ km s}^{-1}$ of the expected location of the HI 21 cm line. Additional data cubes were made at lower spatial resolutions, using smaller UV upper limits. For example, the cube made using visibilities with a UV upper limit of $15 \text{ k}\lambda$ (and Briggs weighting scheme, with $\text{robust} = 1.0$) has a spatial resolution of $7.4'' \times 6.5''$ and an RMS noise of $\approx 280 \mu\text{Jy beam}^{-1}$ per 21.8 km s^{-1} velocity channel. Both the data cubes are CLEANed down to 1.5 times the rms noise in each channel.

As mentioned earlier, the central square baselines ($< 5 \text{ k}\lambda$) of GMRT were not used for making the spectral cubes. The largest angular scale probed by these cubes is thus $\approx 40''$. Hence, the HI 21 cm emission can be reliably mapped

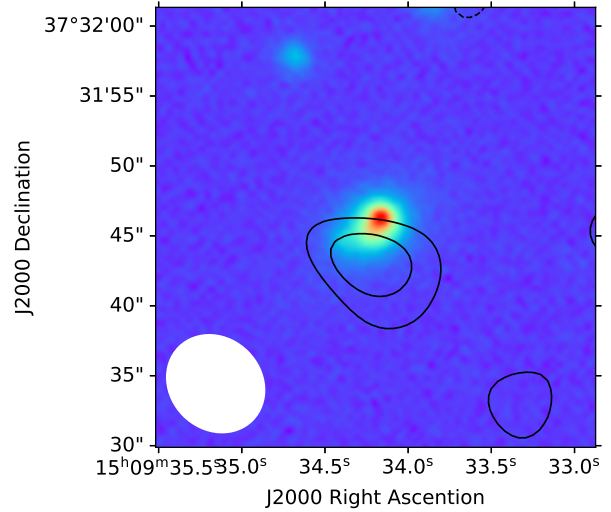


Figure 3. The HI contours at a resolution of $7.4'' \times 6.5''$ overlaid on the DESI Legacy Survey g-band image: The contour levels are at 2, and 3 times the RMS noise in the HI 21 cm map at this resolution. The negative contours are shown in dashed lines. The synthesized beam is shown at the bottom left corner.

up to angular scales of $\lesssim 20''$ (spatial scales of $\lesssim 15$ kpc at the redshift of BB10).

3 HI PROPERTIES OF BB10

HI 21 cm emission from BB10 is detected in our data cube (at $2.9'' \times 2.9''$ angular resolution). The HI 21 cm spectrum was obtained by spatially integrating over the source. The HI 21 cm emission (moment-0) map was obtained by averaging six velocity channels within the FWHM of the HI 21 cm line (also above 1σ). Figure 2[A] shows the HI 21 cm emission map of BB10, overlaid on the DESI Legacy Survey g-band image, and Figure 2[B] shows its HI 21 cm spectrum at a velocity resolution of 21.8 km s^{-1} . The integrated HI 21 cm flux density is $S_{21} = 60 \pm 11 \text{ mJy km s}^{-1}$, which yields an HI mass of $M_{\text{HI}} = (3.12 \pm 0.57) \times 10^8 M_{\odot}$. At an angular resolution of $2.9'' \times 2.9''$, the HI 21 cm emission map has a 2σ column density sensitivity of $N_{\text{HI}} = 1.9 \times 10^{21} \text{ cm}^{-2}$.

The HI 21 cm spectra and emission maps obtained from data cubes made at coarser spatial resolution yield HI masses consistent with the above estimate. The HI 21 cm emission map at a spatial resolution of $7.4'' \times 6.5''$ is shown in Figure 3, which has a 2σ column density sensitivity of $N_{\text{HI}} = 0.7 \times 10^{21} \text{ cm}^{-2}$. Table 2 compiles the details of integrated HI 21 cm flux density, HI mass, and 2σ HI column density for different beam sizes. As the central square baselines are not included, it could not be possible to consider a bigger synthesized beam and make data cubes with coarser resolution. Therefore, our estimate for the HI mass is formally a lower limit of the actual HI mass of the galaxy.

Due to the lack of short baselines, our observations are not sensitive to HI emission on spatial scales $\gtrsim 15$ kpc. However, we note that the non-detection of HI 21cm emission from BB10 with the GBT by K21 and the associated upper limit on its HI mass suggest that the galaxy does not have a significant amount of HI at larger spatial scales. The GBT

⁷ <https://www.cv.nrao.edu/nvss/>

Beam (" × ")	S_{int} (mJy km s ⁻¹)	M_{HI} (× 10 ⁸ M _⊙)	N_{HI} (× 10 ²¹ cm ⁻²)
2.9 × 2.9	60 ± 11	3.12 ± 0.57	1.9
7.4 × 6.5	68 ± 14	3.53 ± 0.73	0.7

Table 2. The values of HI mass (M_{HI}) and 2σ HI column density sensitivity (integrated over the HI 21 cm emission line with velocity width ≈ 130.8 km s⁻¹) at different angular resolutions.

upper limit — $M_{\text{HI}} < 4.4 \times 10^8 M_{\odot}$ — and the (remarkably) tight HI mass–size relation (Wang et al. 2016) suggests a HI disk size (diameter) of $d_{\text{HI}} \lesssim 15$ kpc. It thus appears unlikely that the actual HI mass of BB10 is significantly larger than our estimate.

The HI depletion timescale, $t_{\text{dep}} = M_{\text{HI}}/SFR$, indicates how long a galaxy can continue forming stars without refilling its gas reservoir. BB10 has a short HI depletion timescale of ≈ 0.2 Gyr.

An offset of $2.88'' \pm 0.70''$, i.e. 1.94 ± 0.48 kpc, is seen between the peak of the optical emission and the peak of HI distribution⁸. The HI contours are elongated along the optical extension (see Figure 2[A]). The offset is seen in the HI 21 cm maps at coarser spatial resolutions as well. This offset is significantly larger than the offset between the peak of optical emission and that of radio continuum emission (see Figure 1).

4 DISCUSSION

We compare the HI properties of BB10 with the BBs from K21. We note that BB10 was also included in the sample of K21. Out of a sample of 40 BBs, K21 provide estimates of HI masses for 19 HI detections and upper limits for the remaining 21 including BB10. Our HI mass estimate for BB10 is consistent with the upper limit provided by K21 ($4.4 \times 10^8 M_{\odot}$). Figure 4 shows the HI-to-stellar mass ratio, M_{HI}/M_{*} , and the HI depletion timescale, $t_{\text{dep}} = M_{\text{HI}}/SFR$, against the stellar mass and O32 ratio for the BBs from the sample of K21 along with BB10. The grey filled circles represent the HI detections and the grey downward arrows show the upper limits for the non-detections from K21. In all four panels, BB10 is shown as a blue star. As can be seen in the top left and bottom left panels of Figure 4, BB10 has a somewhat similar HI-to-stellar mass ratio and HI depletion timescale as the BBs from K21 with similar stellar masses. However, it is on the lower side of the HI-to-stellar mass ratio and HI depletion timescale distribution. The top right and bottom right panels of Figure 4 show, as also noted by K21, that galaxies with higher O32 values have preferentially lower HI-to-stellar mass ratio, and thus also typically lower depletion timescales. Our estimates of the HI-to-stellar mass ratio and HI depletion timescale of BB10 are consistent with this scenario. We note that BB10 has a higher O32 ratio than the other BBs with HI 21 cm detections in the K21 sample. However, more measurements of the HI properties of galaxies in the low M_{*} - high O32 space are needed to make a robust conclusion.

⁸ The peak of the HI distribution was localized by fitting a 2D Gaussian to the emission source in the moment-0 map.

Purkayastha et al. (2022) find HI 21 cm emission from a broken ring-like structure around a BB galaxy and suggest a merger event, with a companion galaxy separated by ≈ 4.7 kpc, to be responsible for the starburst activity in that BB galaxy. Recently, Le Reste et al. (2023) present HI imaging of a well-studied local LyC emitter (LCE), Haro 11. Both these studies highlight that mergers can cause a significant displacement of the neutral gas which can facilitate the escape of Lyman- α and possibly also Lyman-continuum photons.

We do not find any clear evidence of a close companion galaxy (or a merging galaxy) from the DESI Legacy Survey (Dey et al. 2019) optical image of BB10. However, as mentioned earlier, we do notice a clear spatial offset between the peak of the HI 21 cm emission and the star-forming region (the brightest part of the optical emission). In addition, the HI distribution extends over the star-forming region as well. We note that optical emission in the DESI image also appears asymmetric as can be seen in Figure 1. While the brightest part of the optical emission is offset from the densest part of the HI spatial distribution, an extended ‘tail’ of the optical emission coincides with the peak of the HI distribution (see Figure 2[A]). Both of these might be caused by a dwarf-dwarf merger. And in that case, BB10 is perhaps in a late-stage merger where the two galaxies have nearly coalesced with each other. Interestingly, the COS-NUV image of BB10, which has a higher spatial resolution than the DESI image, shows relatively extended emission with two or more UV emitting knots within the bright optical emission (see Figure 3 in Jaskot et al. 2019). It is well known that mergers can trigger a starburst (e.g., Luo, Yang, & Zhang 2014; Knapen & Cisternas 2015; Stierwalt et al. 2015; Moreno et al. 2021). Thus a dwarf-dwarf merger scenario can altogether explain the origin of the offset in HI 21 cm emission, multiple UV knots, and the origin of the starburst in BB10.

Finally, compact starbursts can have strong outflows due to stellar/supernova-driven feedback (e.g., Weiner et al. 2009; Heckman et al. 2011; Chisholm et al. 2017). Such outflows can push significant amounts of gas from the star-forming knot of BB10 leading to a paucity of gas in that region.

Using a sample of $z \sim 0.3$ high O32 star-forming galaxies, Izotov et al. (2018) propose an empirical relation between $\Delta v_{\text{Ly}\alpha}$ and the escape fraction of LyC photons ($f_{\text{esc}}^{\text{LyC}}$). Further, Flury et al. (2022) using a multi-parameter analysis finds that $\Delta v_{\text{Ly}\alpha}$ is the best in-direct indicator of $f_{\text{esc}}^{\text{LyC}}$. BB10 has properties which lie within the range of galaxies studied in Izotov et al. (2018), in terms of the O32 ratio, stellar mass, metallicity, SFR, etc. We can thus get an indirect estimate of $f_{\text{esc}}^{\text{LyC}}$ from the observed $\Delta v_{\text{Ly}\alpha} = 400 \pm 27$ km s⁻¹ from Jaskot et al. (2019) and the empirical relation from Izotov et al. (2018). We find an indirect $f_{\text{esc}}^{\text{LyC}} \approx 0.034$ for BB10. Thus BB10 is a weak Ly α and possibly a weak LyC leaker. Indeed mergers can lead to favourable conditions such as triggering an intense starburst (and thus increasing the intrinsic LyC production) and simultaneously displacing a significant amount of HI gas through tidal interactions to open low column density channels which can facilitate the leakage of Ly α and possibly LyC photons (Witten et al. 2024). However, HI 21 cm imaging of a sample of BBs would be needed to help us obtain a better understanding of the role of galaxy mergers, in particular the complex

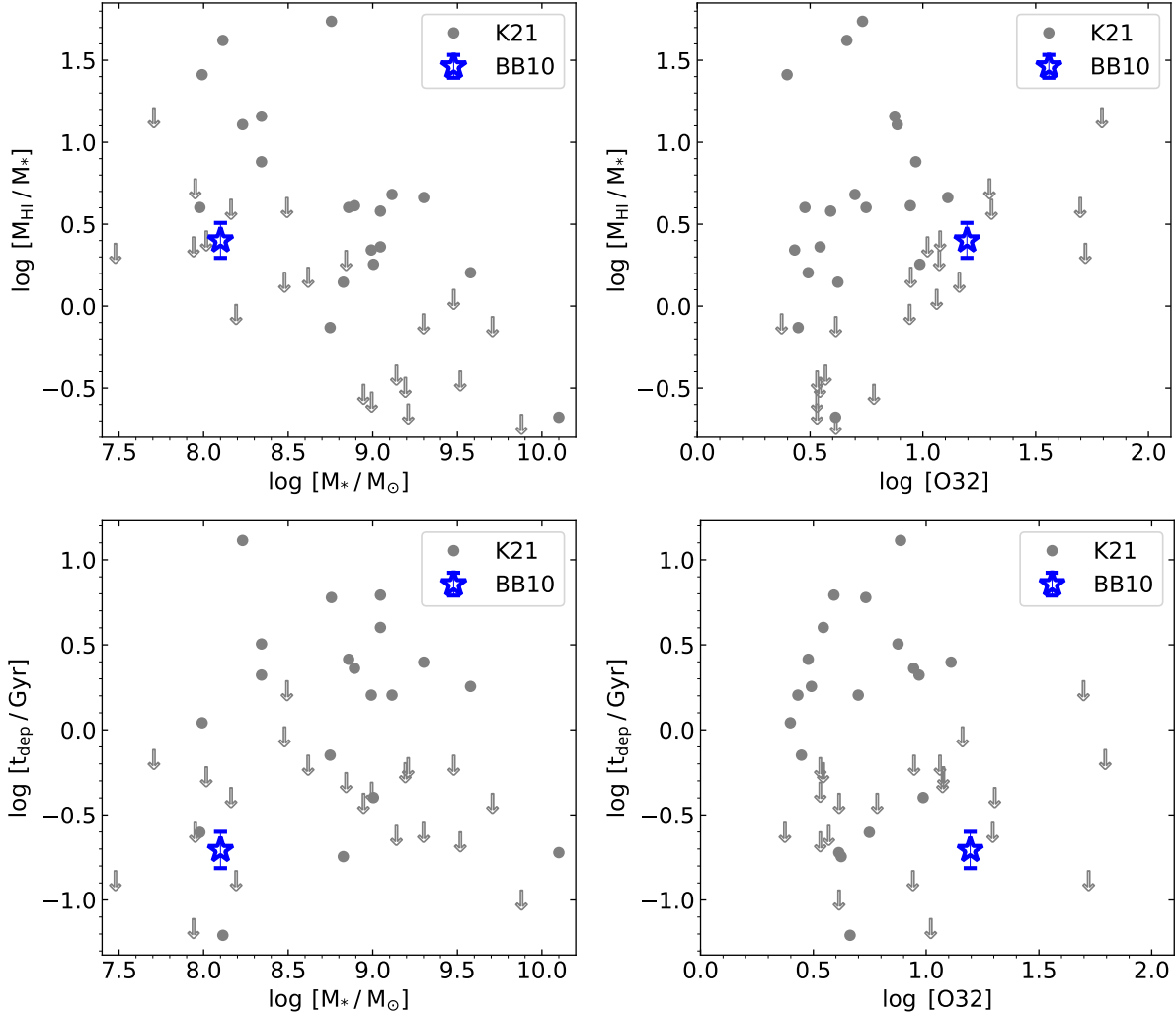


Figure 4. M_{HI}/M_* [top panels] and HI depletion time scale [bottom panels] of galaxies from K21 and BB10 as functions of their stellar mass [left] and O32 [right]: The grey filled circles show HI 21 cm detections of Blueberry galaxies and the grey arrows show 3σ upper limits for non-detections from Kanekar et al. (2021). The blue star represents BB10.

role of orientation and geometrical effects, in the escape of LyC photons. Targeted simulations of merging galaxies with realistic feedback will also be helpful in understanding the role of mergers in LyC escape from these young star-forming galaxies (e.g., Renaud, Bournaud, & Duc 2015).

5 CONCLUSION & SUMMARY

In this article, we present the results obtained from HI 21 cm imaging of a Blueberry galaxy at a redshift of $z = 0.03259$, using uGMRT band-5 receivers. This Blueberry galaxy has an HI mass of $M_{\text{HI}} = (3.12 \pm 0.57) \times 10^8 M_\odot$, and an HI -to-stellar mass ratio $M_{\text{HI}}/M_* \approx 2.4$. Using SFR estimates from the $\text{H}\beta$ emission line (Yang et al. 2017b), we find that it has a short HI depletion time scale of ≈ 0.2 Gyr. Comparing the HI 21 cm emission map with the DESI Legacy Survey optical image of BB10, we find an offset of (1.94 ± 0.48) kpc between the centres of HI 21 cm emission and star-forming region. Such an offset could be a sign of a merger event which can also trigger a starburst. Our study along with Purkayastha

et al. (2022) and Le Reste et al. (2023) highlight the role of dwarf galaxy mergers in the leakage of ionizing photons, and thus their role in cosmic reionization.

ACKNOWLEDGMENTS

We are grateful to the anonymous reviewer and the editor for feedback and suggestions on the manuscript which have improved the article significantly. We thank the staff of the GMRT who have made these observations possible. The GMRT is run by the National Center for Radio Astrophysics of the Tata Institute of Fundamental Research. O. B. is supported by the *AstroSignals* Sinergia Project funded by the Swiss National Science Foundation. S.D and C.A.N. also acknowledge the Department of Atomic Energy for funding support, under project 12-R&D-TFR-5.02-0700.

The Legacy Surveys consist of three individual and complementary projects: the Dark Energy Camera Legacy Survey (DECaLS; Proposal ID #2014B-0404; PIs: David Schlegel and Arjun Dey), the Beijing-Arizona Sky Survey

(BASS; NOAO Prop. ID #2015A-0801; PIs: Zhou Xu and Xiaohui Fan), and the Mayall z-band Legacy Survey (MzLS; Prop. ID #2016A-0453; PI: Arjun Dey). DECaLS, BASS and MzLS together include data obtained, respectively, at the Blanco telescope, Cerro Tololo Inter-American Observatory, NSF's NOIRLab; the Bok telescope, Steward Observatory, University of Arizona; and the Mayall telescope, Kitt Peak National Observatory, NOIRLab. Pipeline processing and analyses of the data were supported by NOIRLab and the Lawrence Berkeley National Laboratory (LBNL). The Legacy Surveys project is honored to be permitted to conduct astronomical research on Iolkam Du'ag (Kitt Peak), a mountain with particular significance to the Tohono O'odham Nation.

NOIRLab is operated by the Association of Universities for Research in Astronomy (AURA) under a cooperative agreement with the National Science Foundation. LBNL is managed by the Regents of the University of California under contract to the U.S. Department of Energy.

This project used data obtained with the Dark Energy Camera (DECam), which was constructed by the Dark Energy Survey (DES) collaboration. Funding for the DES Projects has been provided by the U.S. Department of Energy, the U.S. National Science Foundation, the Ministry of Science and Education of Spain, the Science and Technology Facilities Council of the United Kingdom, the Higher Education Funding Council for England, the National Center for Supercomputing Applications at the University of Illinois at Urbana-Champaign, the Kavli Institute of Cosmological Physics at the University of Chicago, Center for Cosmology and Astro-Particle Physics at the Ohio State University, the Mitchell Institute for Fundamental Physics and Astronomy at Texas A&M University, Financiadora de Estudos e Projetos, Fundacao Carlos Chagas Filho de Amparo, Financiadora de Estudos e Projetos, Fundacao Carlos Chagas Filho de Amparo a Pesquisa do Estado do Rio de Janeiro, Conselho Nacional de Desenvolvimento Cientifico e Tecnologico and the Ministerio de Ciencia, Tecnologia e Inovacao, the Deutsche Forschungsgemeinschaft and the Collaborating Institutions in the Dark Energy Survey. The Collaborating Institutions are Argonne National Laboratory, the University of California at Santa Cruz, the University of Cambridge, Centro de Investigaciones Energeticas, Medioambientales y Tecnologicas-Madrid, the University of Chicago, University College London, the DES-Brazil Consortium, the University of Edinburgh, the Eidgenossische Technische Hochschule (ETH) Zurich, Fermi National Accelerator Laboratory, the University of Illinois at Urbana-Champaign, the Institut de Ciencies de l'Espai (IEEC/CSIC), the Institut de Fisica d'Altes Energies, Lawrence Berkeley National Laboratory, the Ludwig Maximilians Universitat Munchen and the associated Excellence Cluster Universe, the University of Michigan, NSF's NOIRLab, the University of Nottingham, the Ohio State University, the University of Pennsylvania, the University of Portsmouth, SLAC National Accelerator Laboratory, Stanford University, the University of Sussex, and Texas A&M University.

BASS is a key project of the Telescope Access Program (TAP), which has been funded by the National Astronomical Observatories of China, the Chinese Academy of Sciences (the Strategic Priority Research Program "The Emergence of Cosmological Structures" Grant # XDB09000000), and

the Special Fund for Astronomy from the Ministry of Finance. The BASS is also supported by the External Cooperation Program of Chinese Academy of Sciences (Grant # 114A11KYSB20160057), and Chinese National Natural Science Foundation (Grant # 12120101003, # 11433005).

The Legacy Survey team makes use of data products from the Near-Earth Object Wide-field Infrared Survey Explorer (NEOWISE), which is a project of the Jet Propulsion Laboratory/California Institute of Technology. NEOWISE is funded by the National Aeronautics and Space Administration.

The Legacy Surveys imaging of the DESI footprint is supported by the Director, Office of Science, Office of High Energy Physics of the U.S. Department of Energy under Contract No. DE-AC02-05CH1123, by the National Energy Research Scientific Computing Center, a DOE Office of Science User Facility under the same contract; and by the U.S. National Science Foundation, Division of Astronomical Sciences under Contract No. AST-0950945 to NOAO.

DATA AVAILABILITY

Raw data used in this work are available in the GMRT Online Archive (<http://naps.ncra.tifr.res.in/goa/>) under proposal ID: DDT095. Reduced data are available with the corresponding author and will be shared on reasonable request.

REFERENCES

- Abazajian, K. N., et al. 2009, *ApJS*, 182, 543
- Alam S., Albareti F. D., Allende Prieto C., Anders F., Anderson S. F., Anderton T., Andrews B. H., et al., 2015, *ApJS*, 219, 12.
- Albareti F. D., Allende Prieto C., Almeida A., Anders F., Anderson S., Andrews B. H., Aragón-Salamanca A., et al., 2017, *ApJS*, 233, 25.
- Amorín R. O., Pérez-Montero E., Vílchez J. M., 2010, *ApJL*, 715, L128.
- Amorín R., Pérez-Montero E., Vílchez J. M., Papaderos P., 2012, *ApJ*, 749, 185.
- Bouwens R. J., Illingworth G. D., Oesch P. A., Trenti M., Labbé I., Bradley L., Carollo M., et al., 2015, *ApJ*, 803, 34.
- Cameron A. J., Saxena A., Bunker A. J., D'Eugenio F., Carniani S., Maiolino R., Curtis-Lake E., et al., 2023, [arXiv:2302.04298](https://arxiv.org/abs/2302.04298).
- Cardamone C., Schawinski K., Sarzi M., Bamford S. P., Bennert N., Urry C. M., Lintott C., et al., 2009, *MNRAS*, 399, 1191.
- Chisholm J., Orlitová I., Schaerer D., Verhamme A., Worseck G., Izotov Y. I., Thuan T. X., et al., 2017, *A&A*, 605, A67.
- Condon J. J., 1997, *PASP*, 109, 166.
- Condon J. J., Cotton W. D., Greisen E. W., Yin Q. F., Perley R. A., Taylor G. B., Broderick J. J., 1998, *AJ*, 115, 1693.
- Dayal P., Volonteri M., Choudhury T. R., Schneider R., Trebitsch M., Gnedin N. Y., Atek H., et al., 2020, *MNRAS*, 495, 3065.

- Dey A., Schlegel D. J., Lang D., Blum R., Burleigh K., Fan X., Findlay J. R., et al., 2019, *AJ*, 157, 168.
- Drake A. B., Garel T., Wisotzki L., Leclercq F., Hashimoto T., Richard J., Bacon R., et al., 2017, *A&A*, 608, A6.
- Dressler A., Henry A., Martin C. L., Sawicki M., McCarthy P., Villaneuva E., 2015, *ApJ*, 806, 19.
- Finkelstein S. L., Rhoads J. E., Malhotra S., Pirzkal N., Wang J., 2007, *ApJ*, 660, 1023.
- Flury S. R., Jaskot A. E., Ferguson H. C., Worseck G., Makan K., Chisholm J., Saldana-Lopez A., et al., 2022, *ApJ*, 930, 126.
- Gawiser E., Francke H., Lai K., Schawinski K., Gronwall C., Ciardullo R., Quadri R., et al., 2007, *ApJ*, 671, 278.
- Heckman T. M., Borthakur S., Overzier R., Kauffmann G., Basu-Zych A., Leitherer C., Sembach K., et al., 2011, *ApJ*, 730, 5.
- Heintz K. E., Giménez-Arteaga C., Fujimoto S., Brammer G., Espada D., Gillman S., González-López J., et al., 2023, *ApJL*, 944, L30.
- Heintz K. E., Watson D., Brammer G., Vejlggaard S., Hutter A., Strait V. B., Matthee J., et al., 2023, *arXiv*, [arXiv:2306.00647](https://arxiv.org/abs/2306.00647).
- Henry A., Scarlata C., Martin C. L., Erb D., 2015, *ApJ*, 809, 19.
- Izotov Y. I., Guseva N. G., Thuan T. X., 2011, *ApJ*, 728, 161.
- Izotov Y. I., Orlitová I., Schaerer D., Thuan T. X., Verhamme A., Guseva N. G., Worseck G., 2016, *Natur*, 529, 178.
- Izotov Y. I., Schaerer D., Thuan T. X., Worseck G., Guseva N. G., Orlitová I., Verhamme A., 2016, *MNRAS*, 461, 3683.
- Izotov Y. I., Schaerer D., Worseck G., Guseva N. G., Thuan T. X., Verhamme A., Orlitová I., et al., 2018, *MNRAS*, 474, 4514.
- Izotov Y. I., Schaerer D., Worseck G., Verhamme A., Guseva N. G., Thuan T. X., Orlitová I., et al., 2020, *MNRAS*, 491, 468.
- Jaskot A. E., Oey M. S., 2014, *ApJL*, 791, L19.
- Jaskot A. E., Dowd T., Oey M. S., Scarlata C., McKinney J., 2019, *ApJ*, 885, 96.
- Jiang T., Malhotra S., Rhoads J. E., Yang H., 2019, *ApJ*, 872, 145.
- Kanekar N., Ghosh T., Rhoads J., Malhotra S., Harish S., Chengalur J. N., Jones K. M., 2021, *ApJL*, 913, L15.
- Knapen J. H., Cisternas M., 2015, *ApJL*, 807, L16.
- Le Reste A., Cannon J. M., Hayes M. J., Inoue J. L., Kepley A. A., Melinder J., Menacho V., et al., 2023, *MNRAS*.tmp.
- Lintott C. J., Schawinski K., Slosar A., Land K., Bamford S., Thomas D., Raddick M. J., et al., 2008, *MNRAS*, 389, 1179.
- Lofthouse E. K., Houghton R. C. W., Kaviraj S., 2017, *MNRAS*, 471, 2311.
- Luo W., Yang X., Zhang Y., 2014, *ApJL*, 789, L16.
- Malhotra S., Rhoads J. E., Finkelstein S. L., Hathi N., Nilsson K., McLinden E., Pirzkal N., 2012, *ApJL*, 750, L36.
- Matthee J., Mackenzie R., Simcoe R. A., Kashino D., Lilly S. J., Bordoloi R., Eilers A.-C., 2022, *arXiv*, [arXiv:2211.08255](https://arxiv.org/abs/2211.08255).
- McKinney J. H., Jaskot A. E., Oey M. S., Yun M. S., Dowd T., Lowenthal J. D., 2019, *ApJ*, 874, 52.
- McMullin J. P., Waters B., Schiebel D., Young W., Golap K., 2007, *ASPC*, 376, 127.
- Mohan N., Rafferty D., 2015, *ascl.soft*, [ascl:1502.007](https://ascl.soft.1502.007)
- Moreno J., Torrey P., Ellison S. L., Patton D. R., Bottrell C., Bluck A. F. L., Hani M. H., et al., 2021, *MNRAS*, 503, 3113.
- Nakajima K., Ouchi M., Shimasaku K., Ono Y., Lee J. C., Foucaud S., Ly C., et al., 2012, *ApJ*, 745, 12.
- Nakajima K., Ouchi M., 2014, *MNRAS*, 442, 900.
- Nakajima K., Ellis R. S., Robertson B. E., Tang M., Stark D. P., 2020, *ApJ*, 889, 161.
- Planck Collaboration, Aghanim N., Akrami Y., Ashdown M., Aumont J., Baccigalupi C., Ballardini M., et al., 2020, *A&A*, 641, A6.
- Purkayastha S., Kanekar N., Chengalur J. N., Malhotra S., Rhoads J., Ghosh T., 2022, *ApJL*, 933, L11.
- Renaud F., Bournaud F., Duc P.-A., 2015, *MNRAS*, 446, 2038.
- Rhoads J. E., Wold I. G. B., Harish S., Kim K. J., Pharo J., Malhotra S., Gabrielpillai A., et al., 2023, *ApJL*, 942, L14.
- Sebastian B., Bait O., 2019, *ApJL*, 882, L19.
- Schaerer D., Marques-Chaves R., Barrufet L., Oesch P., Izotov Y. I., Naidu R., Guseva N. G., et al., 2022, *A&A*, 665, L4.
- Stierwalt S., Besla G., Patton D., Johnson K., Kallivayalil N., Putman M., Privon G., et al., 2015, *ApJ*, 805, 2.
- Wang J., Koribalski B. S., Serra P., van der Hulst T., Roychowdhury S., Kamphuis P., Chengalur J. N., 2016, *MNRAS*, 460, 2143.
- Weiner B. J., Coil A. L., Prochaska J. X., Newman J. A., Cooper M. C., Bundy K., Conselice C. J., et al., 2009, *ApJ*, 692, 187.
- Witten C., Laporte N., Martin-Alvarez S., Sijacki D., Yuan Y., Haehnelt M. G., Baker W. M., et al., 2024, *NatAs*, 8, 384.
- Yang H., Malhotra S., Gronke M., Rhoads J. E., Dijkstra M., Jaskot A., Zheng Z., et al., 2016, *ApJ*, 820, 130.
- Yang H., Malhotra S., Gronke M., Rhoads J. E., Leitherer C., Wofford A., Jiang T., et al., 2017, *ApJ*, 844, 171.
- Yang H., Malhotra S., Rhoads J. E., Wang J., 2017, *ApJ*, 847, 38.